

Ordered arrays of magnetic nanowires investigated by polarized small-angle neutron scattering

Thomas Maurer

*Laboratoire de Nanotechnologie et d'Instrumentation Optique,
ICD CNRS UMR STMR 6279, Université de Technologie de Troyes,
12 rue Marie Curie, CS 42060, 10004 Troyes Cedex, France*

Sébastien Gautrot, Frédéric Ott, Grégory Chaboussant*

Laboratoire Léon Brillouin, UMR12 CEA-CNRS, 91191 Gif-sur-Yvette, France

Fatih Zighem

LSPM, CNRS-Université Paris XIII, Sorbonne Paris Cité, 93430 Villetaneuse, France

Laurent Cagnon, Olivier Fruchart

Institut Néel, CNRS et Université Joseph Fourier, BP166, F-38042 Cedex 9 Grenoble, France

Polarized small-angle neutron scattering (PSANS) experimental results obtained on arrays of ferromagnetic Co nanowires ($\phi \approx 13$ nm) embedded in self-organized alumina (Al_2O_3) porous matrices are reported. The triangular array of aligned nanowires is investigated as a function of the external magnetic field with a view to determine experimentally the real space magnetization $\vec{M}(\vec{r})$ distribution inside the material during the magnetic hysteresis cycle. The observation of field-dependent SANS intensities allows us to characterize the influence of magnetostatic fields. The PSANS experimental data are compared to magnetostatic simulations. These results evidence that PSANS is a technique able to address real-space magnetization distributions in nanostructured magnetic systems. We show that beyond structural information (shape of the objects, two-dimensional organization) already accessible with nonpolarized SANS, using polarized neutrons as the incident beam provides information on the magnetic form factor and stray fields $\mu_0 H_d$ distribution in between nanowires.

I. INTRODUCTION

The structural, magnetic, and optical properties of nanoobjects organized in periodic arrays have been intensively studied in recent years, as part of the growing interest in functionalized magnetic nanostructures. Several converging lines of effort have greatly improved our knowledge of magnetic nano-objects over the last years. It started with the development of a wide range of systems, from dots to wires, with well controlled structural and magnetic features, and foreseen applications in medicine and magnetoelectronics [1–3].

In this respect, “elongated” magnetic nano-objects in the form of nanowires (or nanorods) with very high aspect ratio (length/radius) have emerged as some of the most promising materials due to several factors [4]. First, synthesis improvements based on self-organization principles have made it possible to produce arrays of very high quality with narrow size distribution [5] and two-dimensional (2D) organization in matrices [6,7]. Second, the magnetic properties of ferromagnetic (FM) nanowires are essentially governed by their shape anisotropy, leading to large magnetic coercivity [8,9], and hence potential for electronic devices or high-density storage, and even high temperature permanent magnets [10]. The understanding of these nanosized systems calls for advanced characterization techniques with high sensitivity and spatial resolution [11] such as a-SNOM (“apertureless” scanning near-field optical microscopy) [12–14], spin-polarized STM [15], electronic holography [16], XMCD-PEEM (x-ray magnetic circular dichroism with photoemission electron microscopy) [17], SPLEEM (spin-polarized low-energy electron microscopy) [18], etc. Most of these techniques are real-space and local, so that complementary approaches should be developed to address the properties of large assemblies of nano-objects either deposited on surfaces or buried in layers. Raman spectroscopy, Brillouin light scattering, x-ray scattering, and neutron scattering (diffraction for structures, inelastic for excitations, and SANS for large-scale objects) are techniques of choice in this regard. The latter technique benefits greatly from a wide available q range. Finally, large theoretical and numerical efforts [19–21] to address fundamental issues related to the transition

*Electronic address: gregory.chaboussant@cea.fr

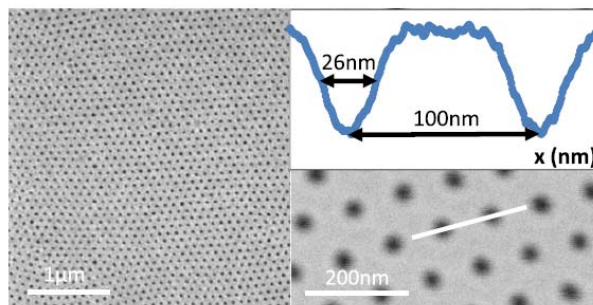


Figure 1: SEM images of the porous alumina membrane used to produce the Co nanowires, and extraction by contrast image treatment of the depth profile of the pores as seen by SEM. The apparent average diameter is estimated to be around 26 nm, but the “surface” diameter is closer to 50 nm, reflecting both a potential conical shape of the pores and also a bias due to the techniques employed to extract the size (image contrast).

from an atomic description to a “nanoscale” description, from discrete approaches to continuous models, have helped us understand the collective behavior of nanoscale objects, in particular magnetic nanowires [22–24].

In this article, we report small-angle neutron scattering with polarized neutrons (PSANS) investigations of ferromagnetic Co nanowires embedded in an alumina matrix. This technique is well suited to probe both the size and shape of nano-objects through the characterization of the form factors (magnetic and nuclear), and their spatial organization through the structure factor. Among all the synthesis strategies, nanowires electrochemically grown inside porous alumina matrices are ideal candidates to test PSANS as they produce triangular arrays with long-range coherence. Only recently, there were reported PSANS studies of magnetic nanowires [25–27]. In particular, Napolskii et al. [27] suggested that the magnetic contribution to SANS could only be explained by taking into account magnetostatic fields between the nanowires. We show in this paper that using polarized neutrons as the incident beam provides information on the magnetic form factor and stray fields $\mu_0 H_d$ distribution.

II. COBALT MAGNETIC NANOWIRES: SYNTHESIS AND BULK MAGNETIC PROPERTIES

The porous alumina membranes are first formed using a double anodization process. The synthesis starts from a bulk Al plate which is electrochemically oxidized to form alumina, Al_2O_3 . During the process, the alumina layer forms self-organized, spatially ordered nanopores whose diameters and interpore distances vary from a few tens of nanometers up to hundreds of nanometers. The different steps involved in the synthesis of porous alumina membranes are extensively documented in Refs. [28–34]. Once the alumina porous layer is formed and after Au deposition (150 nm in thickness) on one surface to act as an electrode, one can fill by electrodeposition the pores with various 3d metals (Fe, Co, Ni) and alloys (CoPt, FePt, FeNi, CoNi) to obtain an array of nano-objects with diameters in the range 10-100 nm and lengths up to several tens of μm [35,36]. The growth process is controlled either by the applied current (galvanostatic deposition) or the applied potential (potentiostatic deposition), and influenced by electrolyte pH [6,37].

In particular, it is possible to synthesize hcp Co nanowires with the \vec{c} axis either parallel or perpendicular to the long axis of the nanowires (for hcp, the preferential growth has the c axis perpendicular to the nanowire axis and, in such a case, there is a competition between the magneto-crystalline anisotropy field and the shape anisotropy field leading to a global coercivity decrease). From scanning electron microscopy (SEM) images, the pores are characterized by their average apparent diameter $\phi_P = 26$ nm and interpore distance $d_P = 105$ nm (see Fig. 1). We argue below that SANS studies may give slightly different results due to the fact that SANS averages the signal over the depth of the wires whereas SEM images give a blurred surface view of the top of the nanowires.

In our case, Co nanowires have been electrodeposited from a solution based on boric acid in which cobalt sulfate and potassium thiocyanate salts have been added. The length of the produced Co nanowires is about 15 μm and they exhibit an amorphous and/or nanocrystallized structure due to the incorporation of thiocyanate ions (known to strongly interact with noble and transition metals [38]) during the growth. Therefore, magnetocrystalline anisotropy is expected to be absent, and only the wire and sample global shape anisotropy will contribute to the hysteresis loop [39]. Transmission electron microscopy (TEM) images show that the pores are well filled and the Co part of the nanowires is homogeneous, which tends to prove that the scattering length density (SLD) can be considered constant across the section of the wires. Magnetic hysteresis cycles for magnetic fields applied parallel (\vec{z} direction) or perpendicular to the

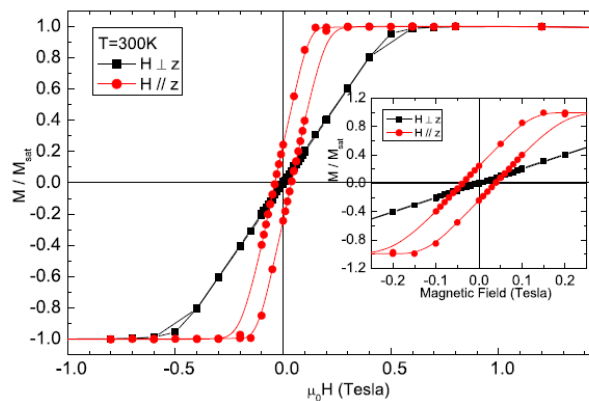


Figure 2: Room temperature VSM (vibrating sample magnetometer) measurements of an array of amorphous Co nanowires (thiocyanate SCN^-) in their alumina matrix measured along the nanowire axis ($\vec{H} \parallel \vec{z}$) and in the plane of the membrane ($\vec{H} \perp \vec{z}$): $\mu_0 H_C^{\parallel} = 38$ mT, $M_R^{\parallel} = 0.25 M_S$ and $\mu_0 H_C^{\perp} = 3.7$ mT, $M_R^{\perp} = 0.008 M_S$.

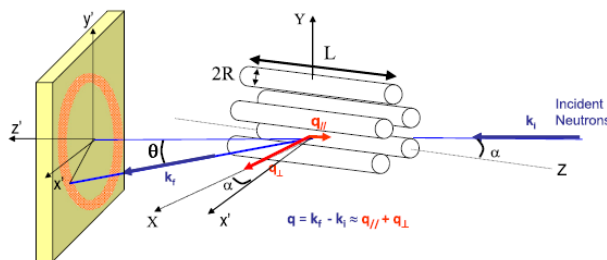


Figure 3: Schematics of the SANS experiments on oriented nanowires (length L and radius R). α is defined as the angle between the cylinder axis (Z axis) and the incident beam direction \vec{k}_i ($k_i = 2\pi/\lambda$). The scattering vector $\vec{q} = \vec{k}_f - \vec{k}_i \approx k_i \sin \theta$ can be expressed in the small-angle approximation [$\cos \theta \approx 1$] as $\vec{q} = \vec{q}_{\parallel} - \vec{q}_{\perp}$ with $\vec{q}_{\parallel} = q \sin \alpha \hat{Z}$ (component along Z) and $\vec{q}_{\perp} = q \cos \alpha \hat{X}$ (component along X).

wires' axes are presented in Fig. 2. For $\vec{H} \perp \vec{z}$, the hysteresis cycle is closed ($\mu_0 H_C^{\perp} = 3.7$ mT and $M_R^{\perp} = 0.008 M_S$). For $\vec{H} \parallel \vec{z}$, the remanence is only $M_R^{\parallel} = 0.25 M_S$ and the coercive field is $\mu_0 H_C^{\parallel} = 38$ mT. Under the assumption that each wire is at any moment mostly uniformly magnetized, and switches abruptly with a finite coercivity, the reduced remanence M_R^{\parallel} and slanted shape of the loop results from the interwire magnetostatic interactions, whose strength is to first order measured by the slanting [40–42]. Domain formation at lowfields is possible and cannot be a priori discarded; however, the actual model to describe the SANS data shown hereafter will still stand even in this case, as only the amplitude of the magnetic form factor may change and not the structure factor nor the nuclear form factor.

III. PSANS INTENSITY: FORM AND STRUCTURE FACTORS

A. General expressions

The PSANS intensity $I^{\pm}(q)$ (\pm stands for up or down incoming polarization with respect to the applied magnetic field) for a perfectly polarized beam may be written with good approximation as:

$$I^{\pm}(q) = |F_N(q) \pm F_M(q)|^2 S(q) \quad (1)$$

where $F_N(q)$, $F_M(q)$ and $S(q)$ are respectively the nuclear and magnetic form factors, and the structure factor, of the scattering objects. The scattering vector modulus q is defined as $q = k_i \sin \theta$, where $k_i = 2\pi/\lambda$ and θ denotes the scattering angle (see Fig. 3). The structure factor $S(q)$ gives access to the spatial correlations between the objects. The nuclear form factor $F_N(q)$ depends on the nuclear scattering length density (SLD) contrast ρ between

the different chemical elements present in the sample (wires plus matrix) and on the geometrical form factor $F_{geo}(q)$ which is governed by the shape of the objects. The magnetic form factor $F_M(q)$ has an expression related to the local magnetization $\vec{M}(\vec{r})$ which will be detailed below. We define $\Sigma I(q)$ and $\Delta I(q)$ as:

$$\Sigma I(q) = I^+(q) + I^-(q) = 2 [F_N^2(q) + F_M^2(q)] S(q) \quad (2)$$

and

$$\Delta I(q) = I^+(q) - I^-(q) = 4F_N(q)F_M(q)S(q) \quad (3)$$

In a real situation, the neutron polarization ratio P is smaller than 1 (usually in the range 0.9 – 0.95 depending on the setup) and thus we must consider mixing channels between up and down beams so that the expected $I_r^+(q)$ and $I_r^-(q)$ become:

$$I_r^+(q) = \frac{1}{2} (1 + P) I^+(q) + \frac{1}{2} (1 - P) I^-(q) \quad (4)$$

and

$$I_r^-(q) = \frac{1}{2} (1 - P) I^+(q) + \frac{1}{2} (1 + P) I^-(q) \quad (5)$$

B. Nuclear form factors $F_N(q)$

In the case of particles of volume V_P with a SLD ρ_P dispersed in a medium with SLD ρ_{med} , the nuclear form factor $F_N(q)$ of the particles is defined as:

$$F_N(\vec{q}) = (\rho_P - \rho_{med}) \int_{V_P} e^{-i\vec{q}\cdot\vec{r}} d\vec{r} = (\Delta\rho) F_{geo}(\vec{q}) \quad (6)$$

where $F_{geo}(\vec{q})$ is the geometrical form factor for one single nanowire, depending only upon the shape and dimensions of the particle, and $\Delta\rho = \rho_P - \rho_{med}$.

1. Uniform cylinder

The geometrical form factor $F_{geo}(\vec{q})$ of one nanowire is, to a very good approximation, equal to that of a filled cylinder of radius R and length L . Assuming the nanowire axis, defined as the Z axis, makes an angle α with respect to the incident beam direction \vec{k}_i , then the geometrical form factor of a cylinder is expressed as [43–45]:

$$F_{geo,cyl}(\vec{q}) = V_P \frac{2J_1(q_\perp R)}{q_\perp R} \cdot \frac{\sin(\frac{1}{2}q_\parallel L)}{\frac{1}{2}q_\parallel L} \quad (7)$$

where $J_1(x)$ is the first-order Bessel function. The longitudinal and transverse components of \vec{q} ($= \vec{q}_\parallel + \vec{q}_\perp$) are $\vec{q}_\parallel = q \sin \alpha \hat{Z}$ and $\vec{q}_\perp = q \cos \alpha \hat{X}$ (see Fig. 3). In the case of perfect alignment between \vec{k}_i and the Z axis ($\alpha = 0, q_\parallel = 0$), $F_{geo,cyl}(\vec{q})$ is simply:

$$F_{geo,cyl}(\vec{q}, \alpha = 0) = V_P \frac{2J_1(q_\perp R)}{q_\perp R} \quad (8)$$

This is similar to the scattering of a flat disk, as the length L of the nanowires has no influence. The alignment process is an important aspect of SANS experiments on elongated ordered objects such as nanowires. For imperfect alignment or radius variation (roughness, interwire distributions), the expression must take into account the length L , the dispersion in α , and R values as shown by Pépy et al. (SAXS) [43] and Marchal et al. (SANS) [44]. Noticeably, the length L will play a role in the stray field spatial distribution (and thus on the PSANS intensity) in a regime where the aspect ratio $L/D = 1-10$, but this is not the case here ($L/D \geq 100$), where we have extremely homogeneous stray field distribution (see Fig. 2 in Ref. [46]).

2. Core-shell cylinder

The form factor for a “core-shell” cylinder (defined by a cylinder of core radius R and core length L with shell thickness t and total length $L + 2t$) is given by [47]:

$$F_N(\vec{q}) = 2(\rho_{core} - \rho_{shell}) V_{core} J_0 \left(q \frac{L}{2} \sin \alpha \right) \frac{J_1(u)}{u} + 2(\rho_{shell} - \rho_{med}) V_{shell} J_0 \left(q \left(t + \frac{L}{2} \right) \sin \alpha \right) \frac{J_1(v)}{v} \quad (9)$$

where $u = qR \cos \alpha$ and $v = q(R + t) \cos \alpha$. ρ_{core} , ρ_{shell} , and ρ_{med} are the SLDs of the core, the shell, and the medium, respectively, and $J_0(x) = \frac{\sin(x)}{x}$.

C. Magnetic form factors $F_M(q)$

The magnetic form factor $F_M(\vec{q})$ for a magnetic atom is defined as:

$$F_M(\vec{q}) = \frac{\gamma r_0}{2V} \int \vec{\sigma} \cdot \vec{M}_\perp(\vec{r}) e^{i\vec{q} \cdot \vec{r}} d\vec{r} \quad (10)$$

where $r_0 = \frac{e^2}{m_e c^2}$ and $\gamma/2 = -1.91$ are respectively the electron radius and the Landé factor for neutrons. $\vec{\sigma}$ is the Pauli operator of $s = 1/2$ neutrons. $F_M(\vec{q})$ is thus proportional to the Fourier transform of the component of \vec{M} perpendicular to the scattering vector \vec{q} , that is the magnetization component parallel to the nanowire axis in the particular case where the nanowires are oriented along the incident beam direction \vec{k}_i (\vec{q} is essentially normal to \vec{k}_i). In analogy with the nuclear SLD, the magnetic SLD for an assembly of magnetic atoms can be written:

$$\rho_M = \frac{e^2 \gamma}{2m c^2} \sum_i c_i M_i^\perp \quad (11)$$

where c_i is the atomic concentration of the i th species and $\frac{e^2 \gamma}{2m c^2} = 0.27 \times 10^{-12}$ cm. The definition of the magnetic form factor for one atom [Eq. (10)], can be extended to a magnetic particle of volume V_i by introducing the magnetic contrast density between the magnetic particles and their a priori nonmagnetic surrounding medium $\Delta\rho_M = \rho_{M,i} - \rho_{M,med}$:

$$F_M(\vec{q}) = \int_{V_i} \Delta\rho_M e^{i\vec{q} \cdot \vec{r}} d\vec{r} \quad (12)$$

where the sum is over the particle’s volume. Assuming that the “surroundings” are nonmagnetic, $\rho_{M,med} = 0$, then we have:

$$F_M(\vec{q}) = \int_{V_i} \rho_{M,i} e^{i\vec{q} \cdot \vec{r}} d\vec{r} \quad (13)$$

We now consider that the field is applied along the nanowire axis and that the magnetic field is sufficiently strong so that the magnetization inside the nanowires is identical for all nanowires and uniform inside the volume of all nanowires ($\rho_{M,i} = \rho_M, \forall i$). This assumption seems perfectly valid at high fields (above 0.5 T according to Fig. 2) but may lose its validity at much smaller fields. Then we can take the SLD term ρ_M out of the integral and we obtain:

$$F_M(\vec{q}) = \rho_M \int_{V_i} e^{i\vec{q} \cdot \vec{r}} d\vec{r} = \rho_M F_{geo}(\vec{q}) \quad (14)$$

where $F_{geo}(\vec{q})$ depends solely on the particle’s shape. $F_M(\vec{q})$ and $F_N(\vec{q})$ are thus related as:

$$F_M(\vec{q}) = \frac{\rho_M}{\Delta\rho} \frac{V_i}{V_p} F_N(\vec{q}) = \chi(\vec{q}) F_N(\vec{q}) \quad (15)$$

where V_i and V_p are the particle’s magnetic volume and the particle’s structural volume, respectively. We make here this distinction to emphasize the difference between magnetic neutron scattering (sensitive to V_i) and nuclear neutron

scattering (sensitive to V_P). Obviously, the parameter $\chi(\vec{q})$ (in units of μ_B) can be simplified when identifying the structural particle volume and its magnetic analog ($V_P = V_i = \pi R^2 L \approx 1.32 \times 10^{-14} \text{ cm}^3$), and with SLD's $\rho_{Co} = 2.26 \times 10^{10} \text{ cm}^{-2}$ (density 8.9 g.cm^{-3}), $\rho_{Al_2O_3} = 4.88 \times 10^{10} \text{ cm}^{-2}$ (density 3.4 g.cm^{-3}), and particle density $c_i \approx \aleph \rho_{Co}/MCo = 9.08 \times 10^{22} \text{ cm}^{-3}$ (\aleph is the Avogadro number), we obtain:

$$\chi \approx -0.936 \sum_i \left(\frac{M_i^\perp}{\mu_B} \right) \quad (16)$$

Various uncertainties may come into play in this estimate: pores which may not be totally filled, the uniformity of the pore dimensions, the effective depth of the membranes, etc., so that an error of 10–15 should be considered. If the magnetization is not uniform inside and/or outside the nanowires, e.g., due to end domains, or stray or demagnetizing fields [27,48,49], then one should consider $\chi(q)$ in its generality:

$$F_M(\vec{q}) = \chi(\vec{q}) F_N(\vec{q}) \quad (17)$$

The function $\chi(\vec{q})$ expresses the spatial distribution of magnetization inside the sample either through SLD variations or effective magnetized volume, and may be extremely complex in the presence of domains, local inhomogeneities, or magnetization gradients for instance.

D. Structure factor $S(q)$

The structure factor $S(q)$ is a consequence of the 2D periodic arrangement of the pores/nanowires in the alumina membrane. A regular and infinite pattern will induce ‘‘Bragg peaks’’ for q values of the associated reciprocal space. SEM images of the porous alumina membranes show a medium- to long-range triangular array with interpore distance d_P around 105 nm and apparent pore diameter ϕ_P around 25–30 nm (see Fig. 1).

$S(q)$ can be evaluated in several ways; numerically from SEM images from which $S(q)$ is obtained by Fourier transform. We found that a Percus-Yevick function is in good agreement with the structure factor as obtained from SEM images. We have adapted a Percus-Yevick model [50,51], originally proposed to describe colloidal particles in liquids, to model $S(q)$ including some disorder in the area of the pores at the membrane's surface. The Percus-Yevick structure factor $S_{PY}(q)$ is written as:

$$S_{PY}(q) \sim (1 - nC(q\phi_S))^{-1} \quad (18)$$

where ϕ_S is the diameter, n is a volume density, and $C(q\phi_S)$ is the radial distribution function. The density number n is related to the packing density parameter η through $n = (6\eta/\pi)\phi_S^{-3}$, which is physically limited by the close-packed solid value $\eta_{max} = \pi 3\sqrt{2} = 0.74$. The correlation function $C(q\phi_S)$ is given by [51]:

$$C(q\phi_S) = -4\pi\phi_S^3 \int_0^1 x^2 J_0(xq\phi_S)(\alpha + \beta x + \gamma x^2) dx \quad (19)$$

with $J_0(u) = \frac{\sin(u)}{u}$, $\alpha = (1 + 2\eta)^2(1-\eta)^{-4}$, $\beta = 6\eta(1 + 0.5\eta)^2(1-\eta)^{-4}$, and $\gamma = 0.5\eta(1 + 2\eta)^2(1-\eta)^{-4}$. Obviously, a Percus-Yevick model is not necessarily adequate to describe an array of disks, but this model turns out to suit the case of partially disordered porous alumina membranes by identifying ϕ_S with the pore diameter ϕ_P . However, the Percus-Yevick model should be applied with some caution in the present case for two reasons: First, the packing density parameter η should not be interpreted as a volume occupation, but rather as an adjustable parameter. Secondly, the validity of the model is dependent upon the quality of the pore ordering. In fact, the more disordered the system is, the better the model fits. For very well ordered systems (triangular with medium range order in the present case), one obtains a diffraction image and the Percus-Yevick model is then less reliable [27]. For assemblies of pores exhibiting some orientational disorder, the Bragg spots are no longer observed at specific q vectors, but the scattering intensity is spread along a ring of constant $|q|$.

Another approach that takes into account the high level of structural order is to consider a 2D triangular lattice with nearest-neighbor interpore spacing d_P ; the structure factor $S_{triang}(q)$ is written as:

$$S_{triang}(q) = \frac{1}{n^2} \sum_p^n \sum_q^n J_0(qd_{pq}) \quad (20)$$

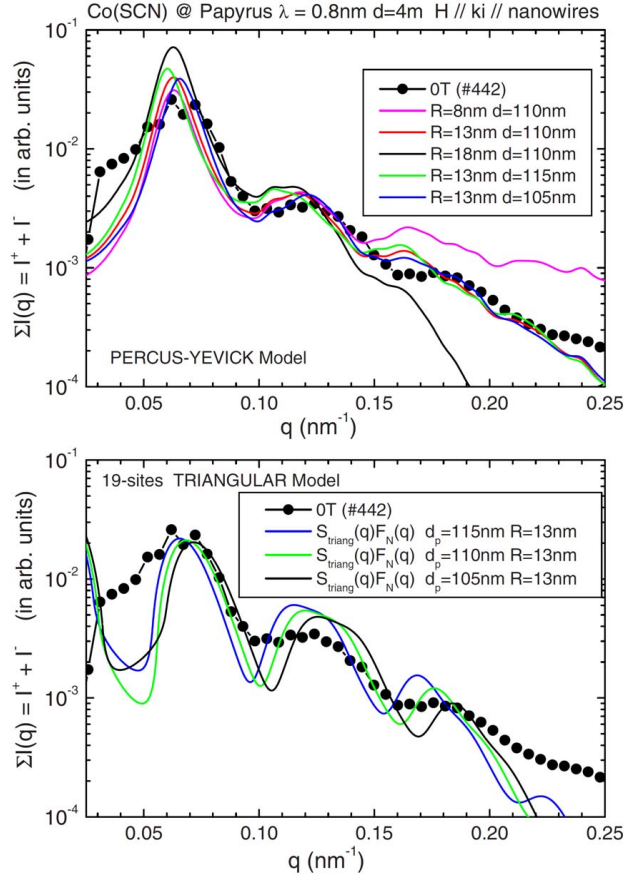


Figure 4: (a) SANS data ($\lambda = 0.8$ nm) compared with a fitted SANS model including a Percus-Yevick structure factor SPY(q) and a Bessel-type expression for the nuclear form factor FN(q). The best agreement is found for $d_P = 110$ nm and $R = 13$ nm (red line). For all fits, η is fixed to 0.5. (b) Triangular array model [Eq. (21)] with $R = 13$ nm fixed and varying interparticle distance d_P . The agreement is correct regarding peak positions but rather poor regarding lineshapes.

where J_0 is the zeroth-order Bessel function. Restricting the sum to nearest neighbors and next-nearest-neighbors on a 2D triangular array, we have:

$$S_{triang}(q) = \frac{1}{361} \left[19 + 168J_0(qd_p) + 54J_0(2qd_p) + 60J_0(\sqrt{3}qd_p) + 36J_0(\sqrt{7}qd_p) + 24J_0(3qd_p) \right] \quad (21)$$

thus matching the reflection positions expected for triangular lattice: $q_{10.0} = q_0 = (2/\sqrt{3})2\pi/d_p$, $q_{00.2} = \sqrt{3}q_0$, $q_{10.1} = 2q_0$, $q_{10.2} = \sqrt{7}q_0$ and $q_{11.0} = 3q_0$.

IV. SANS EXPERIMENTS: RESULTS

The PSANS experiments were performed on the PAPHYRUS (G5.5) spectrometer at the Laboratoire Léon Brillouin (CEA Saclay) with a neutron wavelength of $\lambda = 0.8$ nm and a sample-to-detector distance of 400 cm. The detector is a 64×64 cm² BF₃ 2D grid with 5 mm pixel size (128×128 pixels). The direct beam at the detector (central position) is absorbed by a cadmium beam stopper. The incoming neutrons are polarized in the up (+) direction (vertical direction y' as shown in Fig. 3) by a polarizing mirror to achieve a polarization degree of $P = 0.95$ of the neutrons (determined from reflectivity curves of a reference ferromagnetic thin film). An adiabatic spin flipper reverses the neutron polarization from up (+) to down (-), that is from $+y$ to $-y$. The polarization of the outgoing neutrons hitting the detector is not analyzed. In the present PSANS experiment, the sample (disk of ~ 8 mm diameter) was placed perpendicular to the incoming beam; that is, with Z axis parallel to \vec{k}_i . In such case, $\alpha = 0$ and hence $\vec{q} = \vec{k}_f - \vec{k}_i \approx \vec{q}_\perp$ is a very good approximation. The data are represented as a function of q , which is obtained from the usual SANS expression $q = k_i \sin \theta$ where $k_i = 2\pi/\lambda$ and θ is the scattering angle. Small disorientation of the

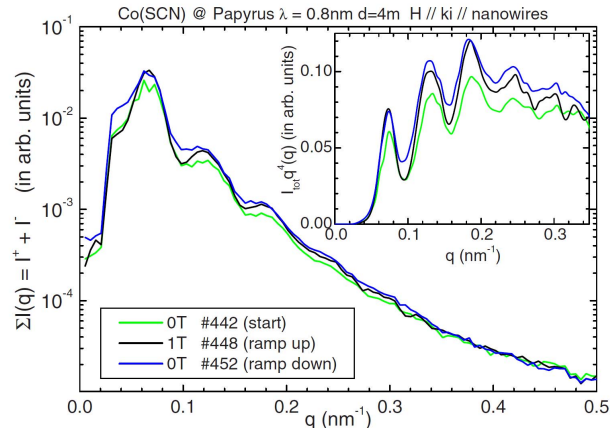


Figure 5: SANS total intensities $\sum I(q) = I^+(q) + I^-(q)$ first measured at 0 T prior to any magnetization of the sample (green curve), then at +1 T (black curve) and finally back at 0 T (blue curve). The inset shows the same data but represented as $\sum I(q)q^4$.

nanowires can contribute so that α marginally deviates from 0, meaning that the SANS data may be dependent on the length of the nanowires. Alignment as good as 0.5° is required to obtain circular “ring-type” SANS scattering. The horizontal magnetic field (7 T superconductor magnet by Oxford Instruments, allowing for relatively large angle scattering ($\pm 10^\circ$)) was set parallel to the incoming beam and hence parallel to the nanowire axis ($\vec{H} \parallel \vec{z}$). The transmitted beam represents only $\approx 20\%$ of the incident beam due to the very strong scattering from the sample. This confirms that such arrays of ordered nanowires strongly interact with the incident wave as shown by Grigoriev et al. [52]. The intensity profile $I(q)$ was obtained after circular integration around the direct beam central position.

Figure 4 shows SANS intensity $I(q)$ of Co nanowires embedded in porous alumina. The first low- q peaks, located at $q \approx 0.065 \text{ nm}^{-1}$ and $q \approx 0.12 \text{ nm}^{-1}$, can serve to estimate the inter-nanowire distance d_P and nanowire radius R . In a first approximation in the triangular lattice case, $d_P = (2/\sqrt{3})(2\pi/0.065) \approx 112 \text{ nm}$, but a more careful estimate is necessary. To this end, we have used the Percus-Yevick model [Eq. (18)]. As shown in Fig. 4, the best agreement is found for $d_P = 110 \text{ nm}$, $R = 13 \text{ nm}$ [the main effect of the radius parameter R is seen by a modification of the $I(q)$ slope at large q] and a packing density parameter $\eta = 0.5$ [53]. The sensitivity to the parameters indicates that errors in the range of 10% are a maximum limit. Introducing inhomogeneous SLD across the wires did not significantly improve the results and might lead to over-parametrization. Therefore, this model appears sufficient to discuss the data. As for comparison between SEM and SANS, it is worth noting that SEM introduces a Gaussian high-frequency noise which corresponds to a spread Gaussian in the reciprocal space, leading to a blurred zone around the holes on the SEM images and preventing an accurate determination of the hole diameter by SEM. Therefore, some caution should be taken when comparing SEM and SANS results. The bottom panel of Fig. 4 shows the results of applying the 19-site triangular 2D model [defined in Eq. (21)] with a various d_P values. The overall agreement is satisfactory concerning the peak positions, however, the relative intensities are poorly described by this model. The agreement in the estimate of the nanowire/pore radius between SANS, which is a bulk technique, and a surface technique like SEM is very good and gives some credit to the interpretation of the SEM images presented earlier. In addition, as discussed below, the “magnetic” radius derived from the present data is also in agreement with the structural radius.

In order to access the magnetic behavior of the Co nanowires, we applied magnetic fields parallel to the long axis of the nanowires and focused on the scattering evolution. Figure 5 shows $\sum I(q) = I^+(q) + I^-(q)$ for three field values: first at 0 T prior to any magnetization of the sample (green curve), then at 1 T (black curve), and finally at 0 T (blue curve). Before discussing the effect of the magnetic field, let us discuss the structure factor peaks. As shown in the inset of Fig. 5, the “high- q ” peaks are much more visible in a $\sum I(q)q^4$ representation showing eventual deviations from the Porod law at large q originating from interface scattering [54]. At least four peaks are clearly visible at $q = 0.073, 0.130, 0.184,$ and 0.244 nm^{-1} , and they correspond well with the values derived from the purely triangular array structure factor model with $d_P = 110 \text{ nm}$ ($q = 0.066, 0.114, 0.132, 0.174, 0.198,$ and 0.228 nm^{-1}). The observed peaks at $q = 0.130$ and 0.184 nm^{-1} are the result of two unresolved peaks at $0.11\text{--}0.13$ and $0.17\text{--}0.2 \text{ nm}^{-1}$. For $d_P = 105 \text{ nm}$ and $d_P = 115 \text{ nm}$, the agreement is significantly worse.

Regarding magnetic field effects, several comments can be made. First there is a significant increase of scattering between 0 and 1 T, characterized by an enhancement of the structure factor peaks and some additional intensities in between the $S(q)$ peaks from 1 T back down to 0 T, which show the importance of magnetic history in this system.

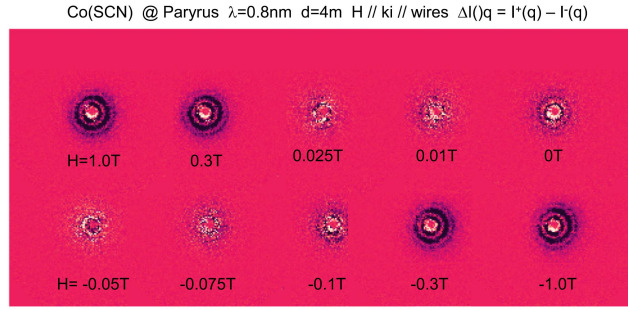


Figure 6: 2D detector maps representing $\Delta I(q) = I^+(q) + I^-(q) \propto F_M(q)$ at 200 K and for several magnetic fields H parallel to the long axis of the cobalt nanowires and to the incident beam direction.

The evolution of the magnetic scattering $\Delta I(q) = I^+(q) + I^-(q) \propto F_M(q)$ as a function of the applied magnetic field is first shown in Fig. 6 as 2D maps of the detector. The observed concentric rings are clearly field dependent, with low magnitude (positive or negative) at low fields and maximized magnitude at large magnetic fields (± 1 T). At intermediate fields, the pattern is more complex and the several visible concentric rings are better represented after a circular integration of the 2D plots. This is represented in Fig. 7 where the color code groups data sets of similar q dependence: high-field ($\mu_0|H| > 0.3$ T) data drawn in black, lowfield data are in green, and blue/red show intermediate magnetic fields. By introducing a scaling factor $K(H)$, $\Delta I(H) \sim K(H)\Delta I(1T)$, where the data at 1 T serve as reference data for “fully magnetized” nanowires along their long axis, one can derive from these curves a hysteretic behavior of $\Delta I(q, H)$ by plotting the scalar $K(H)$ (see inset in Fig. 7) at some chosen q value [herewe choose $q = 0.073 \text{ nm}^{-1}$ which is the position for the largest $\Delta I(q)$ value at 1 T]. While green data are characterized by very low $\Delta I(q)$ values, red and blue $\Delta I(q)$ values are relatively large and, most noticeably, with $K(H)$ values of opposite sign.

After noticing that the structure factor probes only nuclear densities and, therefore, remains unchanged with magnetic field variations, one can infer from Eq. (3) that the observed field-dependence of $\Delta I(q)$ is due to the magnetic form factor $F_M(q)$. The striking feature revealed in the inset of Fig. 7 is the sign inversion of $K(H)$ occurring at ± 50 mT, followed by another more modest inversion below ± 20 mT, which is close to the coercive field value (38 mT, see Fig. 2). It shows that the magnetization component $M_{\perp \vec{q}}$, through the present evolution of $F_M(\vec{q})$, presents inversion features at low fields. To go further in the analysis, it is necessary to eliminate the structure factor $S(q)$ contribution by considering the evolution of $\chi(\vec{q}) = F_M(\vec{q})/F_N(\vec{q})$ [Eq. (17)]. From $\chi(\vec{q})$, one can extract directly $F_M(\vec{q})$ since we know the nuclear form factor $F_N(\vec{q})$ from Eq. (7) (with $q_{\parallel}L \ll 1$):

$$F_M(\vec{q}) = \chi(\vec{q})F_N(\vec{q}) = -0.936 \sum_i \left(\frac{M_i^{\perp}}{\mu_B} \right) (\Delta\rho) V_P \frac{2J_1(q_{\perp}R)}{q_{\perp}R} \quad (22)$$

Knowing $\chi(\vec{q})$ from the PSANS experiments and $F_N(\vec{q})$ (best fits to the unpolarized data and SEM images with $R = 13$ nm as the main parameter), we can plot the magnetic form factor $F_M(\vec{q})$ (see Fig. 8) for three magnetic field values (in chronological order 1 T, 25 mT, and 0 T) corresponding to the three regimes identified in Fig. 7. We then make the assumption that $F_M(\vec{q})$ can be expressed as the product of an amplitude scaling parameter (K') and a geometrical magnetic form factor which represents the magnetic “landscape” of the sample: $F_M(\vec{q}) = K'F_M^{geo}(\vec{q})$. We find that the geometrical magnetic form factor $F_M^{geo}(\vec{q})$ is best modeled using a “core-shell cylinder” type geometrical magnetic form factor [see Eq. (9)]:

$$F_M^{geo}(\vec{q}) = I_1 \frac{J_1(qR_1)}{qR_1} + I_2 \frac{J_1(qR_2)}{qR_2} \quad (23)$$

where R_1 is the core radius and $R_2 = R_1 + t$ is the shell radius. The results are shown in Fig. 8. A very good agreement is found in the three identified regimes with the following parameters: with $I_1 = \Delta\rho_1 V_1 = 2.3 \pm 0.2$, $R_1 = 12.35 \pm 0.15$ nm ($V_1 \approx 500$), $I_2 = \Delta\rho_2 V_2 = 3.6 \pm 0.5$, $R_2 = 31.6 \pm 0.9$ nm ($V_2 \approx 2500$), and K' values as shown in the inset of Fig. 8. Setting arbitrarily $I_2 = 0$ or $I_2 > 0$ leads to a monotonic decrease of $F_M^{geo}(\vec{q})$, in total disagreement with the experimental observation. As an example, the bold green line in Fig. 8 shows the magnetic form factor for $I_2 = 0$. Qualitatively, the position of the main oscillation in $F_M^{geo}(\vec{q})$ is set by $\approx 2\pi/R_2$. The R_1 and R_2 values deserve comment. R_1 is extremely close to the structural nanowire/pore radius (13 nm), indicating

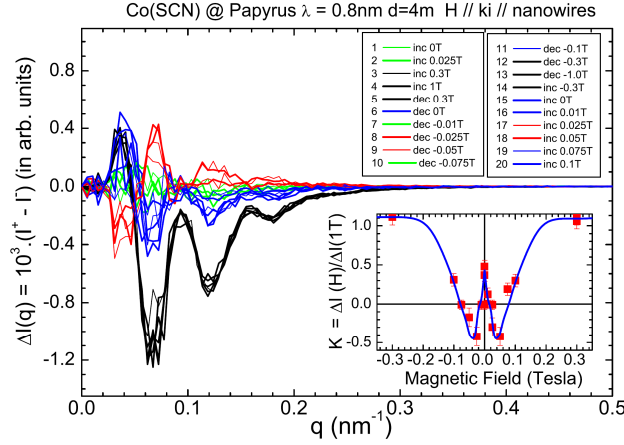


Figure 7: Circular integration of PSANS intensities $\Delta I(q) = I^+(q) + I^-(q) \propto F_M(q)$. The color code groups data sets with the same “shape” or q dependence. High-field ($\mu_0|H| > 0.3$ T) data are in black; low-field data are in green and blue/red show intermediate magnetic fields. As in Fig. 5, the peaks are located at the same q values. The q -oscillatory behavior can be qualitatively expressed as $\Delta I(H) \sim K(H)\Delta I(1T)$ where 1 T data serve a benchmark. While green data are characterized by very low $\Delta I(q)$ values, red and blue $\Delta I(q)$ values are relatively large with reversed sign of K . The inset shows the proportionality term $K(H)$ as a function of magnetic field (hysteresis loop between -1 T and +1 T) obtained from the value of $\Delta I(q)$ at $q = 0.073 \text{ nm}^{-1}$ position for each magnetic field value. The solid line is a guide to the eyes.

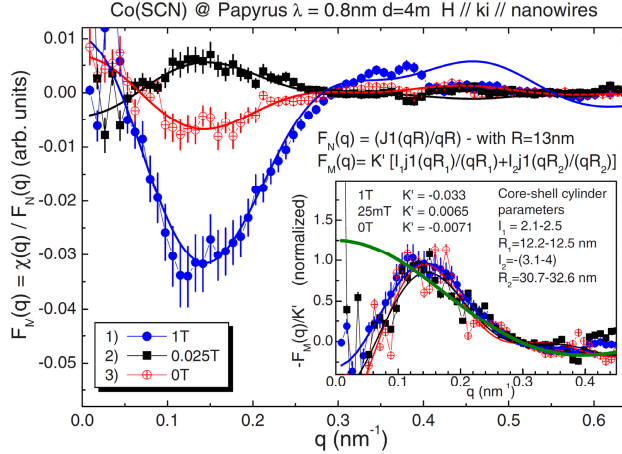


Figure 8: Magnetic form factor $F_M(\vec{q})$ of ferromagnetic Co nanowires for different longitudinal magnetic field fields: In chronological order (1) 1 T, (2) 25 mT, and (3) 0 T. Solid lines are best fits using a core-shell cylinder model with the parameters $I_1 = 2.3 \pm 0.2$, $R_1 = 12.35 \pm 0.15$ nm, $I_2 = 3.6 \pm 0.5$, and $R_2 = 31.6 \pm 0.9$. Inset: $F_M(\vec{q})$ normalized to unity (divided by K'). The scaling parameter K' for each magnetic field is indicated. The green continuous line in the inset panel represents the expected magnetic form factor in the absence of a dipolar shell (i.e., with $I_2 = 0$).

that the “core” magnetization inside the wire extends across all the nanowire volume and that the magnetization is essentially uniform, even for low magnetization values. The “shell” radius, much larger than the structural nanowire radius, $R_2 \approx 31$ nm, reflects the fact that dipolar fields (opposed to the core magnetization) extend in between nanowires. The dipolar field profile $\mu_0 \vec{H}_{dip}(\vec{q})$ may differ strongly depending on the length of the nanowires and on the internanowire distance, the type of packing, the internal magnetization value, etc. [20]. The scaling parameter K' exhibits a surprising field dependence with inversion features at low fields (below 0.1 T) that, seemingly, is not related to the internal magnetization distribution inside/outside the nanowires.

From the core-shell model, one can estimate the magnetic moment induced by the nanowires in the matrix volume around the nanowires:

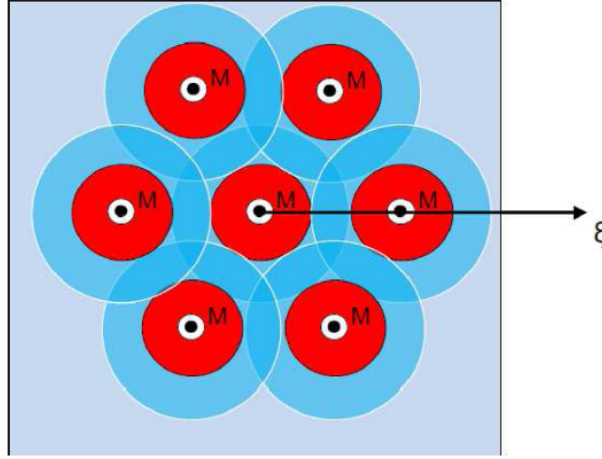


Figure 9: Triangular array of nanowires with homogeneous magnetization inside the core (in red) and dipolar field intensity (in blue). The dipolar field creates a neutron scattering contrast with the non-magnetic matrix. The axis ξ will meet different dipolar field profile depending on its relative orientation. The data obtained will then correspond to a profile average.

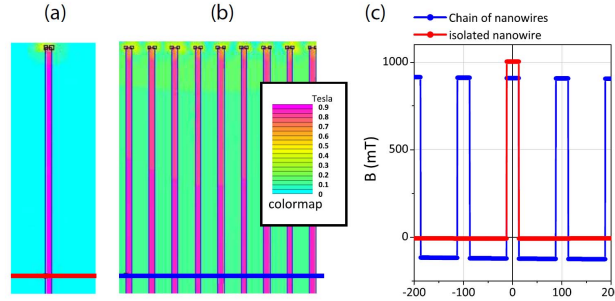


Figure 10: (a) Dipolar fields generated by an individual nanowire with a diameter of 25 nm and a length of 5 μm . (b) Dipolar fields generated for an assembly of nanowires and internanowire distance, center to center, of 100 nm. (c) Profile of the induction for both situations, indicating that the dipolar fields are sizable in magnitude (with reversed sign) relative to the core induction. In the 2D triangular situation [24] the effect is further enhanced. The simulation has been performed with the FEMM software.

$$\gamma_{1,2} = \frac{\rho_{M,1} - \rho_{M,2}}{\rho_{M,2}} = \frac{I_1}{I_2} \times \frac{V_2}{V_1} \quad (24)$$

where the subscripts 1 and 2 relate to the nanowire core and to the outer dipolar field volume, respectively. With $\frac{I_1}{I_2} \approx -0.638$ and $\frac{V_2}{V_1} \sim \left(\frac{R_2}{R_1}\right)^2 \sim 6.54$, we obtain $\rho_{M,1}/\rho_{M,2} = 1 + \gamma_{1,2} \approx -3.17$. The quantity $\rho_{M,1}$ is related to the magnetization component M_i^\perp of the Co atoms, which is, at full saturation, $M_{Co,sat} \approx 1.7\text{--}1.75 \mu_B/(\text{Co atom}) \approx 1400$ kA/m, equivalent to a magnetic field $\mu_0 H_{core}^z \approx 1.7$ T. From the analysis of the experimental data, we would obtain an opposing magnetic field in the shell region around the nanowires of $\mu_0 H_{shell}^z = -\rho_{M,2}/\rho_{M,1} \times \mu_0 H_{core}^z \approx -0.315 \times 1.7 \approx -0.53$ T, as depicted in Fig. 9. In some instances, the demagnetization field can be phenomenologically related to the “porosity” P of the array [55,56]: $H_d \approx -M_{Co,sat}P$. This is equivalent to saying that the demagnetizing field of a regular array of ferromagnetic nanowires is the demagnetizing field of a uniform ferromagnetic film modulated by a porosity factor (surface ratio). With $P = \pi\phi_P^2/(2\sqrt{3}d_P^2) \approx 0.05$, we have $\mu_0 H_d \approx -85$ mT, which is one order of magnitude lower than that derived from PSANS. To back up our findings, we have performed numerical simulations, using the FEMM (Finite Element Method Magnetics) software [57], on nanowires ($2R = 25$ nm, $L = 5$ μm). The FEMM results are shown in Fig. 10: Panel (a) shows a color map of the dipolar field generated by one individual nanowire and a transverse cut of the induction related to the nanowire integrated along z , arising from both magnetization and dipolar fields. Panel (b) shows the same features for a chain of nanowires separated by $4R$. These results clearly indicate that dipolar fields cannot be neglected in the calculation of the induction for an assembly of nanowires. The intensity and local variations of dipolar fields in between nanowires should be taken into

account when it comes to evaluating the magnetic SANS signal. These experimental results confirm the conclusion of a recent study on 2D arrays of ordered Ni nanowires probed by SANS [27] and performed on similar systems but with a magnetic field transverse to the nanowires. They also exhibited results which cannot be explained without considering complex dipolar fields, not only at the end tips of the nanowires but also in between the nanowires ($H_d/H_{core} \approx -0.31$).

V. CONCLUSION

We have performed polarized small-angle neutron scattering (PSANS) on ordered arrays of Co magnetic nanowires. PSANS is a powerful but emerging technique which has only recently been used to investigate the magnetic configuration of nanoparticles. For instance, PSANS revealed chemically uniform, but magnetically distinct, core and canted shell in 9 nm magnetite particles [58]. Here, we show that PSANS is a tool to characterize, both structurally and magnetically, anisotropic magnetic nano-objects. With unpolarized neutrons, it is possible to disentangle the structure factor of the array and the nuclear form factor of a single wire. In previous studies, focused on Co and Ni nanowires ordered in Al_2O_3 membranes but with the external magnetic field applied perpendicular to the wire long axis [25,27,48], the variation of the SANS intensity depending on the applied magnetic field reveals that stray fields have to be taken into account in the magnetic formfactor derivation. In the polarized-neutrons case, we show that it is possible to derive directly from experiment the magnetic form factor, and therefore the magnetization distribution in the sample. We argue that it necessitates the introduction of significant magnetostatic fields in between nanowires, whose effects are modeled using a straightforward core-shell model comprising (1) a core magnetic radius of induction close to the Co value and equal to the structural radius, and (2) a “dipolar shell” induction of constant but opposite amplitude surrounding the core induction. The evolution of these fields as a function of external magnetic field is also reported. Subtle inversion effects at very low fields due to the interplay of internal and external fields have been evidenced. We show that a magnetization “mapping” in such types of nano-objects is indeed possible using PSANS techniques and may easily be extended to further deposited nano-objects (dots, wires, etc.). Such type of studies indicates that PSANS is a promising technique able to provide information about complex magnetization in nano-objects.

-
- [1] O. Fruchart, C. R. Phys. 6, 61 (2005).
 - [2] A. Enders, R. Skomski, and J. Honolka, J. Phys.: Condens. Matter 22, 433001 (2010).
 - [3] B. D. Terris, J. Magn. Magn. Mater. 321, 512 (2009).
 - [4] L. Sun, Y. Hao, C. L. Chien, and P. C. Searson, IBM J. Res. Dev. 49, 79 (2005).
 - [5] Y. Soumare, C. Garcia, Th. Maurer, G. Chaboussant, F. Ott, F. Fievet, J. Y. Piquemal, and G. Viau, Adv. Func. Mater. 19, 1971 (2009).
 - [6] M. Darques, A. Encinas-Oropesa, L. Villa, and L. Piraux, J. Phys. D: Appl. Phys 37, 1411 (2004).
 - [7] S. Da Col, M. Darques, O. Fruchart, and L. Cagnon, Appl. Phys. Lett. 98, 112501 (2011).
 - [8] T. Maurer, F. Ott, G. Chaboussant, Y. Soumare, J.-Y. Piquemal, and G. Viau, Appl. Phys. Lett. 91, 172501 (2007).
 - [9] K. Soulantica, F. Wetz, J. Maynadie, A. Falqui, R. P. Tan, Th. Blon, B. Chaudret, and M. Respaud, Appl. Phys. Lett. 95, 152504 (2009).
 - [10] K. A. Atmane, F. Zighem, Y. Soumare, M. Ibrahim, R. Boubekri, Th. Maurer, J. Margueritat, J. Y. Piquemal, F. Ott, G. Chaboussant, F. Schoenstein, N. Jouini, and G. Viau, J. Solid State Chem. 197, 297 (2013).
 - [11] P. Fischer, T. Eimuller, G. Schutz, G. Denbeaux, A. Pearson, L. Johnson, D. Attwood, S. Tsunashima, M. Kumazawa, N. Takagi, M. Kohler, and G. Bayreuther, Rev. Sci. Instrum. 72, 2322 (2001).
 - [12] B. Knoll and F. Keilmann, Opt. Commun. 182, 321 (2000).
 - [13] L. Gomez, R. Bachelot, A. Bouhelier, G. P. Wiederrecht, S. H. Chang, S. K. Gray, F. Hua, S. Jeon, J. A. Rogers, M. E. Castro, S. Blaize, I. Stefanon, G. Lerondel, and P. Royer, J. Opt. Soc. Am. B 23, 823 (2006).
 - [14] A. Bek, R. Vogelgesang, and K. Kern, Rev. Sci. Instrum. 77, 043703 (2006).
 - [15] M. Bode, Rep. Prog. Phys. 66, 523 (2003).
 - [16] E. Snoeck, C. Gatel, L. M. Lacroix, T. Blon, S. Lachaize, J. Carrey, M. Respaud, and B. Chaudret, Nano Lett. 8, 4293 (2008).
 - [17] E. Bauer, J. Phys.: Condens. Matter 13, 11391 (2001).
 - [18] N. Rougemaille and A. K. Schmid, Eur. J. Phys. A 50, 20101 (2010).
 - [19] R. Hertel, J. Appl. Phys. 90, 5752 (2001).
 - [20] L. Clime, P. Ciureanu, and A. Yelon, J. Magn. Magn. Mater. 297, 60 (2006).
 - [21] M. Bahiana, F. S. Amaral, S. Allende, and D. Altbir, Phys. Rev. B 74, 174412 (2006).
 - [22] D. Laroze, J. Escrip, P. Landeros, D. Altbir, M. Vazquez, and P. Vargas, Nanotechnology 18, 415708 (2007).
 - [23] Th. Maurer, F. Zighem, W. Fang, F. Ott, G. Chaboussant, Y. Soumare, K. A. Atmane, J. Y. Piquemal, and G. Viau, J. Appl. Phys. 110, 123924 (2011).

- [24] F. Zighem, Th. Maurer, F. Ott, and G. Chaboussant, *J. Appl. Phys.* 109, 013910 (2011).
- [25] N. A. Grigoriyeva, S. V. Grigoriev, H. Eckerlebe, A. A. Eliseev, A. V. Lukashin, and K. S. Napolskii, *J. Appl. Crystallogr.* 40, S532 (2007).
- [26] N. A. Grigoriyeva, S. V. Grigoriev, H. Eckerlebe, A. A. Eliseev, A. V. Lukashin, and A. S. Vyacheslavov, *Physica B* 397, 82 (2007).
- [27] K. S. Napolskii, A. P. Chumakov, S. V. Grigoriev, N. A. Grigoriyeva, H. Eckerlebe, A. A. Eliseev, A. V. Lukashin, and Y. D. Tretyakov, *Physica B* 404, 2568 (2009).
- [28] C. R. Martin, *Science* 266, 1961 (1994).
- [29] H. Masuda and K. Fukuda, *Science* 268, 1466 (1995).
- [30] C. R. Martin, *Chem. Mater.* 8, 1739 (1996).
- [31] O. Jessensky, F. Müller, and U. Gösele, *Appl. Phys. Lett.* 72, 1173 (1998).
- [32] O. Rabin, P. R. Herz, Y. M. Lin, A. I. Akinwande, S. B. Cronin, and M. S. Dresselhaus, *Adv. Funct. Mater.* 13, 631 (2003).
- [33] K. Lagrenée and J. M. Zanotti, *Eur. Phys. J. Special Topics* 141, 261 (2007).
- [34] R. C. Furneaux, W. R. Rigby, and A. P. Davidson, *Nature (London)* 337, 147 (1989).
- [35] Y. Dahmane, L. Cagnon, J. Voiron, S. Pairis, M. Bacia, L. Ortega, N. Benbrahim, and A. Kadri, *J. Phys. D: Appl. Phys.* 39, 4523 (2006).
- [36] L. Cagnon, Y. Dahmane, J. Voiron, S. Pairis, M. Bacia, L. Ortega, N. Benbrahim, and A. Kadri, *J. Magn. Magn. Mater.* 310, 2428 (2007).
- [37] M. Darques, L. Piraux, A. Encinas, P. Bayle-Guillemaud, A. Popa, and U. Ebels, *Appl. Phys. Lett.* 86, 072508 (2005).
- [38] C. Rambaud, L. Cagnon, J. P. Lévy, and G. Tourillon, *J. Electrochem. Soc.* 151, E352 (2004).
- [39] This is in contrast to Co nanowires grown under pH = 3.4 (resp. pH = 5.75) which crystallize in the hcp phase with the c axis perpendicular (resp. parallel) to the nanowire axis (z axis).
- [40] A. Encinas-Oropesa, M. Demand, L. Piraux, I. Huynen, and U. Ebels, *Phys. Rev. B* 63, 104415 (2001).
- [41] K. Nielsch, R. B. Wehrspohn, J. Barthel, J. Kirschner, U. Gosele, S. F. Fischer, and H. Kronmüller, *Appl. Phys. Lett.* 79, 1360 (2001).
- [42] M. Vazquez, M. Hernandez-Velez, K. Pirota, A. Asenjo, D. Navas, J. Velazquez, P. Vargas, and C. Ramos, *Eur. Phys. J. B* 40, 489 (2004).
- [43] G. Pépy and A. Kuklin, *Nucl. Instrum. Methods Phys. Res. B* 185, 198 (2001).
- [44] D. Marchal and B. Demé, *J. Appl. Crystallogr.* 36, 713 (2003).
- [45] I. Grillo, *Small-Angle Neutron Scattering and Applications in Soft Condensed Matter* (Springer-Verlag, Berlin, 2008).
- [46] R. Lavin, J. C. Denardin, J. Escrig, D. Altbir, A. Cortés, and H. Gomez, *IEEE Trans. Magn.* 44, 2808 (2008).
- [47] A. Guinier and G. Fournet, *Small-Angle Scattering of X-Rays* (John Wiley and Sons, New York, 1955).
- [48] S. V. Grigoriev, A. P. Chumakov, A. V. Syromyatnikov, N. A. Grigoriyeva, A. I. Okorokova, K. S. Napolskii, I. V. Roslyakov, A. A. Eliseev, A. V. Lukashin, and H. Eckerlebe, *Phys. Solid State* 52, 1080 (2010).
- [49] S. V. Grigoriev, N. A. Grigoriyeva, K. S. Napolskii, A. P. Chumakov, A. A. Eliseev, I. V. Roslyakov, H. Eckerlebe, and A. V. Syromyatnikov, *JETP Lett.* 94, 635 (2011).
- [50] J. K. Percus and G. J. Yevick, *Phys. Rev.* 110, 1 (1958); J. K. Percus, *Phys. Rev. Lett.* 8, 462 (1962).
- [51] N. W. Ashcroft and J. Lekner, *Phys. Rev.* 145, 83 (1966).
- [52] S. V. Grigoriev, A. V. Syromyatnikov, A. P. Chumakov, N. A. Grigoriyeva, K. S. Napolskii, I. V. Roslyakov, A. A. Eliseev, A. V. Petukhov, and H. Eckerlebe, *Phys. Rev. B* 81, 125405 (2010).
- [53] $\eta = 0.5$ works quite well, but relatively good agreement can be found with either $\eta = 0.4$ or $\eta = 0.6$.
- [54] G. Porod, *Small-Angle X-ray Scattering*, edited by O. Glatter and O. Kratky (Academic, New York, 1982).
- [55] C. Z. Li and J. C. Lodder, *J. Magn. Magn. Mater.* 88, 236 (1990).
- [56] J. Meier, B. Doudin, and J.-P. Ansermet, *J. Appl. Phys.* 79, 6010 (1996).
- [57] D. C. Meecker, software Finite Element Method Magnetics, <http://www.femm.info>.
- [58] K. L. Krycka, R. A. Booth, C. R. Hogg, Y. Ijiri, J. A. Borchers, W. C. Chen, S. M. Watson, M. Laver, T. R. Gentile, L. R. Dedon, S. Harris, J. J. Rhyne, and S. A. Majetich, *Phys. Rev. Lett.* 104, 207203 (2010).